Synthetic turbulence, fractal interpolation, and large-eddy simulation

Sukanta Basu,* Efi Foufoula-Georgiou,† and Fernando Porté-Agel†
St. Anthony Falls Laboratory, University of Minnesota, Minneapolis, Minnesota 55414, USA
(Received 16 October 2003; revised manuscript received 6 April 2004; published 31 August 2004)

Fractal interpolation has been proposed in the literature as an efficient way to construct closure models for the numerical solution of coarse-grained Navier-Stokes equations. It is based on synthetically generating a scale-invariant subgrid-scale field and analytically evaluating its effects on large resolved scales. In this paper, we propose an extension of previous work by developing a multiaffine fractal interpolation scheme and demonstrate that it preserves not only the fractal dimension but also the higher-order structure functions and the non-Gaussian probability density function of the velocity increments. Extensive *a priori* analyses of atmospheric boundary layer measurements further reveal that this multiaffine closure model has the potential for satisfactory performance in large-eddy simulations. The pertinence of this newly proposed methodology in the case of passive scalars is also discussed.

DOI: 10.1103/PhysRevE.70.026310 PACS number(s): 47.27.Ak, 47.27.Eq, 47.53.+n

I. INTRODUCTION

Generation of turbulence-like fields (also known as *synthetic turbulence*) has received considerable attention in recent years. Several schemes have been proposed [1–5] with different degrees of success in reproducing various characteristics of turbulence. Recently, Scotti and Meneveau [6,7] further broadened the scope of synthetic turbulence research by demonstrating its potential in computational modeling. Their innovative turbulence emulation scheme based on the *fractal interpolation technique* (FIT) [8,9] was found to be particularly amenable for a specific type of turbulence modeling, known as large-eddy simulation (LES, at present the most efficient technique available for high Reynolds number flow simulations, in which the larger scales of motion are resolved explicitly and the smaller ones are modeled). The underlying idea was to explicitly reconstruct the subgrid (unresolved) scales from given resolved scale values (assuming computation grid-size falls in the *inertial range* of turbulence) using FIT and subsequently estimate the relevant subgrid-scale (SGS) tensors necessary for LES. Simplicity, straightforward extensibility for multidimensional cases, and low computational complexity (appropriate use of *fractal calculus* can even eliminate the computationally expensive explicit reconstruction step, see Sec. IV for details), makes this FIT-based approach an attractive candidate for SGS modeling in LES.

Although the approach of [6,7] is better suited for LES than any other similar scheme (e.g., [1–5]), it falls short in preserving the essential small-scale properties of turbulence, such as multiaffinity (which will be defined shortly) and non-Gaussian characteristics of the probability density function (PDF) of velocity increments. It is the purpose of this work to extend the approach of [6,7] in terms of realistic turbulence-like signal generation with all the aforementioned desirable characteristics and demonstrate its potential for LES through *a priori* analysis (an LES-SGS model evaluation framework). We will also demonstrate the competence of our scheme in the emulation of passive-scalar fields for which the non-Gaussian PDF and multiaffinity are significantly pronounced and cannot be ignored.

II. BASICS OF FRACTAL INTERPOLATION

The fractal interpolation technique is an iterative affine mapping procedure to construct a synthetic deterministic small-scale field (in general fractal provided certain conditions are met, see below) given a few large-scale interpolating points (anchor points). For an excellent treatise on this subject, the reader is referred to the book by Barnsley [9]. In this paper, we will limit our discussion (without loss of generality) only to the case of three interpolating data points: $\{(x_i,\tilde{u}_i), i=0,1,2\}$. For this case, the fractal interpolation iterative function system (IFS) is of the form $\{R^2; w_n, n=1,2\}$, where, w_n have the following affine transformation structure:

$$w_n\begin{pmatrix} x \\ u \end{pmatrix} = \begin{bmatrix} a_n & 0 \\ c_n & d_n \end{bmatrix}\begin{pmatrix} x \\ u \end{pmatrix} + \begin{pmatrix} e_n \\ f_n \end{pmatrix}, n = 1,2. \tag{1}$$

To ensure continuity, the transformations are constrained by the given data points as follows: $w_n\binom{x_0}{\tilde{u}_0}=\binom{x_{n-1}}{\tilde{u}_{n-1}}$ and $w_n\binom{x_2}{\tilde{u}_2}=\binom{x_n}{\tilde{u}_n}$, for $n=1,2$. The parameters $a_n, c_n, e_n,$ and f_n can be easily determined in terms of d_n (known as the vertical stretching factors) and the given anchor points $(x_i,\tilde{u}_i)$ by solving a linear system of equations. The attractor of the above IFS, G, is the graph of a continuous function $u:[x_0,x_2]\rightarrow R$, which interpolates the data points $(x_i,\tilde{u}_i)$, provided the vertical stretching factors d_n obey $0\leqslant|d_n|<1$. In other words,

$$G = \{(x,u(x)): x \in [x_0,x_2]\}, \tag{2}$$

where,

*Electronic address: basus@msi.umn.edu
†Also at the National Center for Earth-Surface Dynamics, 2 3rd Avenue SE, Minneapolis, Minnesota 55414, USA.

$$u(x_i) = \tilde{u}_i, i = 0,1,2.$$

Moreover, if $|d_1|+|d_2|>1$ and $(x_i,\tilde{u}_i)$ are not collinear, then the fractal (box-counting) dimension of G is the unique real solution D of $|d_1|a_1^{D-1}+|d_2|a_2^{D-1}=1$ (for rigorous proof see [8]). In the special case of three equally spaced points covering the unit interval [0,1], i.e., $x_0=0, x_1=0.5$ and $x_2=1$, the parameters of the affine transformation kernel become $a_n=0.5; c_n=(\tilde{u}_n-\tilde{u}_{n-1})-d_n(\tilde{u}_2-\tilde{u}_0); e_n=x_{n-1}; f_n=\tilde{u}_{n-1}-d_n\tilde{u}_0; n=1,2$. In this case, the solution for the fractal dimension (D) becomes

$$D = 1 + \log_2(|d_1| + |d_2|). \tag{3}$$

Notice that the scalings d_1 and d_2 are free parameters and cannot be determined using only Eq. (3); at least one more constraint is necessary. For example, [6,7] chose to use the additional condition $|d_1|=|d_2|$.

III. SYNTHETIC TURBULENCE GENERATION

Not long ago, it was found that turbulent velocity signals at high Reynolds numbers have a fractal dimension of $D \simeq 1.7\pm0.05$, very close to the value of $D=5/3$ expected for Gaussian processes with a $-5/3$ spectral slope [10]. For $D=5/3$, the assumption of $|d_1|=|d_2|$ along with Eq. (3) yields $|d_1|=|d_2|=2^{-1/3}$ [6,7]. One contribution of this paper is a robust way of estimating the stretching parameters without any ad hoc prescription; the resulting synthetic field will not only preserve the fractal dimension (D) but also other fundamental properties of real turbulence.

As an exploratory example, using the fractal interpolation IFS [Eq. (1)], we construct a 2^{17} points long synthetic fractal series, $u(x)$, with given coarse-grained points $(0.0,1.2),(0.5,-0.3)$, and $(1.0,0.7)$ and the stretching parameters used in [6,7]: $d_1=-2^{-1/3}, d_2=2^{-1/3}$. Clearly, Fig. 1(a) depicts that the synthetic series has fluctuations at all scales and it passes through all three interpolating points.

Next, from this synthetic series we compute higher-order structure functions [see Fig. 1(b) for orders 2, 4, and 6], where the qth-order structure function, $S_q(r)$, is defined as follows:

$$S_q(r) = \langle |u(x+r) - u(x)|^q \rangle \sim r^{\zeta_q}, \tag{4}$$

where the angular bracket denotes spatial averaging and r is a separation distance that varies in an appropriate scaling region (known as the inertial range in turbulence). If the scaling exponent ζ_q is a nonlinear function of q, then following the convention of [1–5], the field is called *multiaffine*, otherwise it is termed as *monoaffine*. In this context, we would like to mention that Kolmogorov's celebrated 1941 hypothesis (K41) based on the assumption of global scale invariance in the inertial range predicts that the structure functions of order q scale with an exponent $q/3$ over inertial range separations [11,12]. Deviations from $\zeta_q=q/3$ would suggest inertial range intermittency and invalidate the K41 hypothesis. Inertial range intermittency is still an unresolved issue, although experimental evidence for its existence is overwhelming [11,13]. To interpret the curvilinear behavior

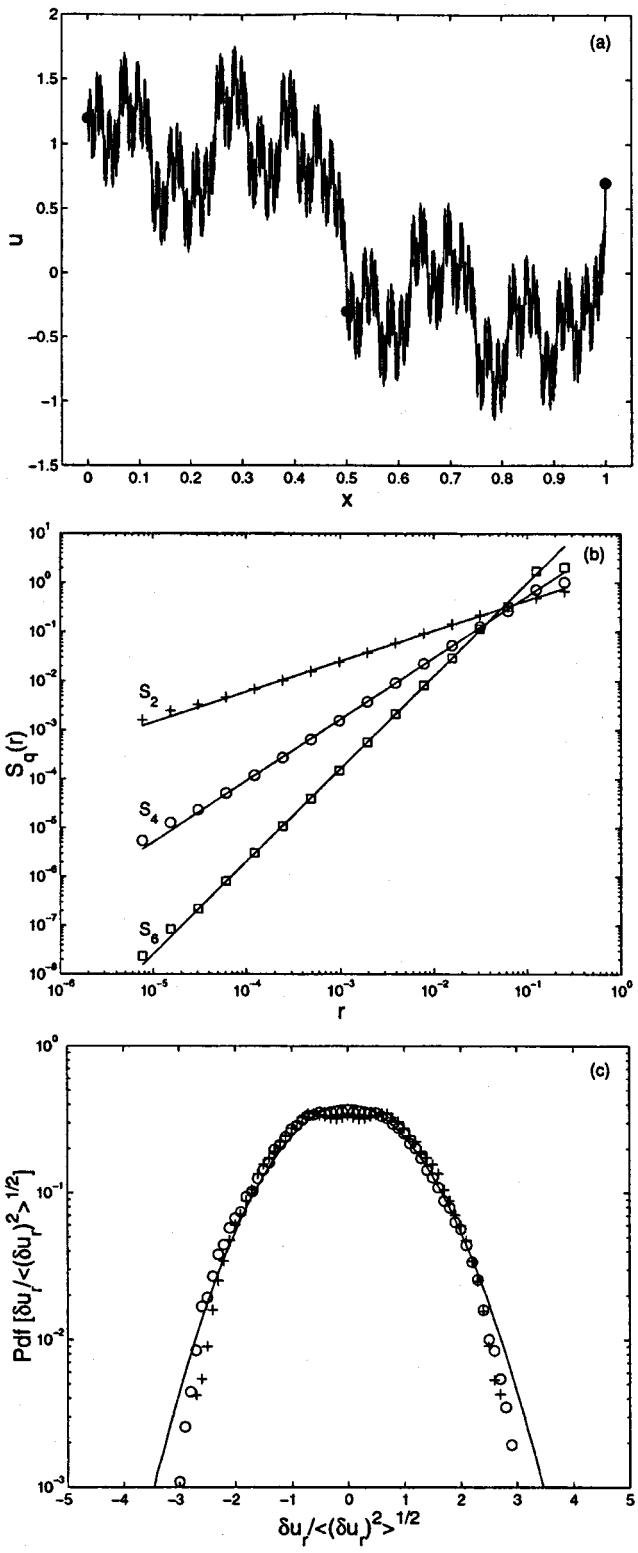

FIG. 1. (a) A synthetic turbulence series of fractal dimension $D=5/3$. The black dots denote initial interpolating points. (b) Structure functions of order 2, 4, and 6 (as labeled) computed from the series in Fig. 1(a). The slopes (ζ_q) corresponding to this particular realization are 0.62, 1.25, and 1.89, respectively. (c) PDFs of the normalized increments of the series in (a). The plus signs correspond to $r=2^{-14}$, while the circles refer to a distance $r=2^{-6}$. The solid curve designates the Gaussian distribution for reference.

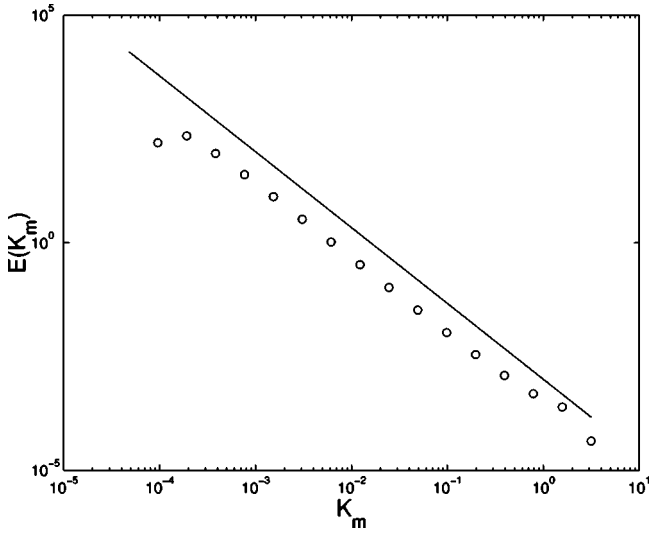

FIG. 2. Wavelet power spectrum (cirlces) of the series in Fig. 1(a). The $-5/3$ power law is also shown for comparison.

of the ζ_q function observed in experimental measurements (e.g., [13]), Parisi and Frisch [12,14] proposed the *multifractal* model, by replacing the global scale invariance with the assumption of local scale invariance. They conjectured that at very high Reynolds number, turbulent flows have singularities (almost) everywhere and showed that the singularity spectrum is related to the structure function-based scaling exponents, ζ_q, by the Legendre transformation.

Our numerical experiment with the stretching parameters of [6,7], i.e., $|d_1|=|d_2|=2^{-1/3}$, revealed that the scaling exponents follow the K41 predictions (after ensemble averaging over 100 realizations corresponding to different initial interpolating points), i.e., $\zeta_q=q/3$ (not shown here), a signature of monoaffine fields. Later on, we will give analytical proof that indeed this is the case for $|d_1|=|d_2|=2^{-1/3}$. Also, in this case, the PDFs of the velocity increments, $\delta u_r(x)=u(x+r)-u(x)$, always portray near-Gaussian (slightly platykurtic) behavior irrespective of r [see Fig. 1(c)]. This is contrary to the observations [11,13], where typically the PDFs of increments are found to be r-dependent and become more and more non-Gaussian as r decreases. Theoretically, non-Gaussian characteristics of PDFs correspond to the presence of intermittency in the velocity increments and gradients (hence in the energy dissipation) [2,5,11,12].

In Fig. 2, we plot the wavelet spectrum of this synthetic series. Due to the dyadic nature of the fractal interpolation technique, the Fourier spectrum will exhibit periodic modulation (see Figs. 7 and 8 of [7]). To circumvent this issue we make use of the (dyadic) discrete Haar wavelet transform. Following [15], the wavelet power spectral density function $E(K_m)$ is defined as

$$E(K_m) = \frac{\langle [W^{(m)}(i)]^2 \rangle dx}{2\pi \ln(2)}, \tag{5}$$

where wave number $K_m(=2\pi/(2^m dx))$ corresponds to scale $R_m(=2^m dx)$. The scale index m runs from 1 (finest scale) to $\log_2(N)$ (coarsest scale). $W^{(m)}(i)$, dx, and N denote the Haar wavelet coefficient at scale m and location i, spacing in physical space and length of the spatial series, respectively. The power spectrum displays the inertial range slope of $-5/3$, as anticipated.

At this point, we would like to invoke an interesting mathematical result regarding the scaling exponent spectrum, ζ_q, of the fractal interpolation IFS [16],

$$\zeta_q = 1 - \log_N \sum_{n=1}^{N} |d_n|^q, \tag{6}$$

where N is the number of anchor points -1 (in our case $N=2$). The original formulation of [16] was in terms of a more general scaling exponent spectrum, $\tau(q)$, rather than the structure-function-based spectrum ζ_q. The $\tau(q)$ spectrum is an exact Legendre tranform of the singularity spectrum in the sense that it is valid for any order of moments (including negative) and any singularities [17,18]. $\tau(q)$ can be reliably estimated from data by the wavelet-transform modulus-maxima method [17,18]. To derive Eq. (6) from the original formulation, we made use of the equality $\tau(q)=\zeta_q-1$, which holds for positive q and for positive singularities of Hölder exponents less than unity [17,18]. In turbulence, the most probable Hölder exponent is 0.33 (corresponding to the K41 value) and for all practical purposes the values of Hölder exponents lie between 0 and 1 (see [19,20]). Hence the use of the above equality is well justified.

Equation (6) could be used to validate our previous claim that the parameters of [6,7] give rise to a monoaffine field (i.e., ζ_q is a linear function of q). If we consider $|d_1|=|d_2|=d=2^{-1/3}$, then $\zeta_q=1-\log_2(|d_1|^q+|d_2|^q)=1-\log_2(2d^q)=-q\log_2(d)=-q\log_2(2^{-1/3})=q/3$ (QED). Equation (6) could also be used to derive the classic result of Barnsley regarding the fractal dimension of IFS. It is well known [21,22] that the graph dimension (or box-counting dimension) is related to ζ_1 as follows: $D=2-\zeta_1$. Now, using Eq. (6) we get $D=2-\zeta_1=1+\log_N \Sigma_{n=1}^{N}|d_n|$. For $N=2$, we recover Eq. (3).

Intuitively, by prescribing several scaling exponents, ζ_q (which are known *a priori* from observational data), it is possible to solve for d_n from the overdetermined system of equations [Eq. (6)]. These solved parameters, d_n, along with other easily derivable (from the given anchor points and d_n) parameters (a_n, c_n, e_n, and f_n) in turn can be used to construct multiaffine signals. For example, solving for the values quoted by Frisch [12]—$\zeta_2=0.70, \zeta_3=1, \zeta_4=1.28, \zeta_5=1.53, \zeta_6=1.77, \zeta_7=2.01$, and $\zeta_8=2.23$, along with $\zeta_1=0.33$ (corresponding to $D=5/3$)—yields the stretching factors $|d_n|=0.887, 0.676$. There are altogether eight possible sign combinations for the above stretching parameter magnitudes and all of them can potentially produce multiaffine fields with the aforementioned scaling exponents. However, all of them might not be the "right" candidate from the LES-performance perspective. Rigorous *a priori* and *a posteriori* testing of these multiaffine SGS models is needed to elucidate this issue (see Sec. V).

We repeated our previous numerical experiment with the stretching parameters $d_1=-0.887$ and $d_2=0.676$. Figure 3(a) shows the measured values (ensemble averaged over 100 re-

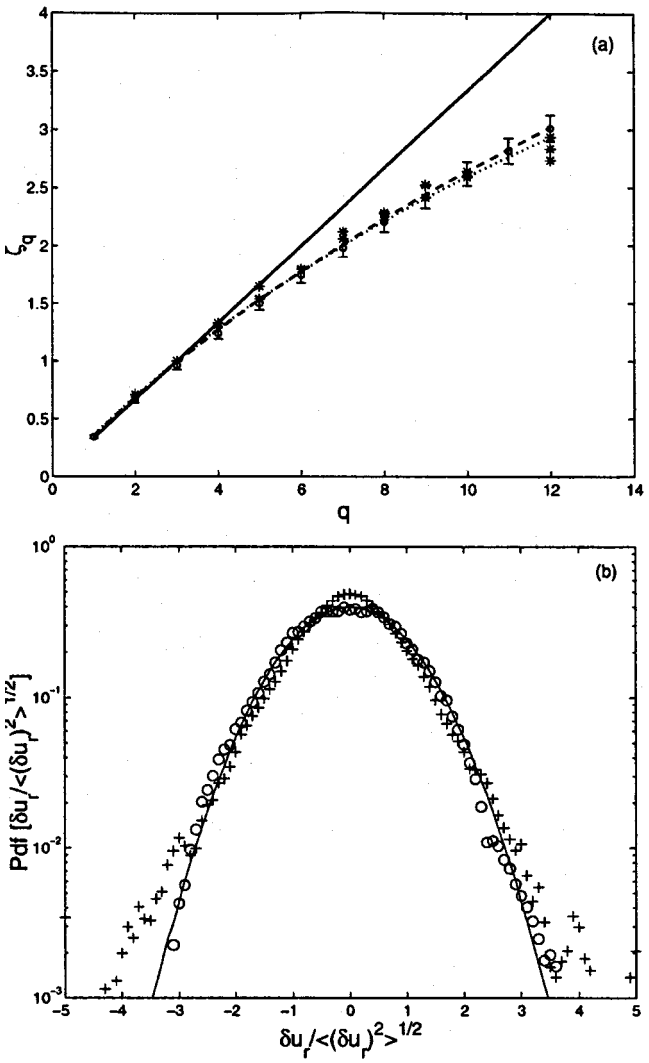

FIG. 3. (a) The scaling exponent function ζ_q. The continuous, dashed, and dotted lines denote the K41, Eq. (6), and the She-Lévêque model predictions, respectively. The circles with error bars (one standard deviation) are estimated values over 100 realizations using $d_1=-0.887$ and $d_2=0.676$. Experimental data of Anselmet *et al.*'s [5] is also shown for reference (star signs). (b) PDFs of the normalized increments of the multiaffine series. The plus signs denote $r=2^{-14}$, while the circles refer to a distance $r=2^{-6}$. The solid curve designates the Gaussian distribution for reference.

alizations) of the scaling exponents ζ_q up to 12th order. For comparison we have also shown the theoretical values computed directly from Eq. (6) (dashed line). A model proposed by She and Lévêque [23] based on a hierarchy of fluctuation structures associated with the vortex filaments is also shown for comparison (dotted line). We chose this particular model because of its remarkable agreement with experimental data. The She and Lévêque model predicts $\zeta_q=q/9+2-2\left(\frac{2}{3}\right)^{q/3}$. Figure 3(b) shows the PDFs of the increments, which are quite similar to what is observed in real turbulence—for large r the PDF is near Gaussian while for smaller r it becomes more and more peaked at the core with high tails [see also Fig. 7(b) for the variation of flatness factors of the PDFs of increments with distance r].

IV. FRACTAL CALCULUS AND SUBGRID-SCALE MODELING

In the case of an incompressible fluid, the spatially filtered Navier-Stokes equations are

$$\frac{\partial \tilde{u}_m}{\partial x_m} = 0, \tag{7a}$$

$$\frac{\partial \tilde{u}_m}{\partial t} + \tilde{u}_n \frac{\partial \tilde{u}_m}{\partial x_n} = -\frac{\partial}{\partial x_n}\left[\frac{\tilde{p}}{\rho}\delta_{mn} + \tau_{mn}\right] + \nu \nabla^2 \tilde{u}_m, \tag{7b}$$

$$m,n = 1,2,3,$$

where t is time, x_n is the spatial coordinate in the n direction, u_n is the velocity component in the n direction, p is the dynamic pressure, ρ is the density, and ν is the molecular viscosity of the fluid. The tilde denotes the filtering operation, using a filter of characteristic width Δ [24]. These filtered equations are now amenable to numerical solution (LES) on a grid with mesh size of order Δ, considerably larger than the smallest scale of motion (the Kolmogorov scale). However, the SGS stress tensor τ_{mn} in Eq. (7b), defined as

$$\tau_{mn} = \widetilde{u_m u_n} - \tilde{u}_m \tilde{u}_n, \tag{8}$$

is not known. It essentially represents the contribution of unresolved scales (smaller than Δ) to the total momentum transport and must be parametrized (via a SGS model) as a function of the resolved velocity field. Due to the strong influence of the SGS parametrizations on the dynamics of the resolved turbulence, considerable research efforts have been made during the past decades and several SGS models have been proposed (see [26,27] for reviews). The eddy-viscosity model [28] and its variants (e.g., the dynamic model [29] and the scale-dependent dynamic model [30]) are perhaps the most widely used SGS models. They parametrize the SGS stresses as being proportional to the resolved velocity gradients. These SGS models and other standard models (e.g., similarity, nonlinear, mixed models) postulate the form of the SGS stress tensors rather than the structure of the SGS fields ([31]). Philosophically a very different approach would be to explicitly reconstruct the subgrid scales from given resolved scale values (by exploiting the statistical structures of the unresolved turbulent fields) using a specific mathematical tool (e.g., the fractal interpolation technique) and subsequently estimate the relevant SGS tensors necessary for LES. The fractal model of [6,7] and our proposed multiaffine model basically represent this new class of SGS modeling, also known as the "direct modeling of SGS turbulence" [26,27,32].

In Sec. III, we have demonstrated that FIT could be effectively used to generate synthetic turbulence fields with desirable statistical properties. In addition, Barnsley's rigorous fractal calculus offers the ability to analytically evaluate any statistical moment of these synthetically generated fields, which in turn could be used for SGS modeling. Detailed discussion of the fractal calculus is beyond the scope of this

paper. Below, we briefly summarize the equations most relevant to the present work. Let us first consider the moment integral: $U_{l,m}=\int_0^1 x^m[u(x)]^l dx$. In the present context ($x_0=0, x_1=0.5,$ and $x_2=1$), this moment integral could be viewed as 2Δ filtering ($\Delta=0.5$) with the top-hat filter [i.e., $F_\Delta(x)=1/\Delta$ if $|x|<\Delta/2$, and $F_\Delta(x)=0$ otherwise]. For instance, the 1D component of the SGS stress tensor reads

$$\tau=\widetilde{uu}-\tilde{u}\tilde{u} \tag{9a}$$

$$=U_{2,0}-U_{1,0}U_{1,0}. \tag{9b}$$

Barnsley [8] proved that for the fractal interpolation IFS [Eq. (1)], the moment integral becomes

$$U_{l,m}=\frac{\left[\sum_{j=0}^{m-1} U_{l,j}\binom{m}{j}\sum_{n=1}^{2} a_n^{j+1}d_n e_n^{m-j}+\sum_{p=0}^{l-1}\sum_{j=0}^{l+m-p} K(l,m,p,j)U_{p,j}\right]}{\left(1-\sum_{n=1}^{2} a_n^{m+1}d_n^l\right)}, \tag{10a}$$

where

$$\sum_{n=1}^{2}\binom{l}{p}a_n(c_n x+f_n)^{l-p}d_n^p(a_n x+e_n)^m=\sum_{j=0}^{l+m-p}K(l,m,p,j)x^j. \tag{10b}$$

After some algebraic manipulations, the SGS stress equation at node x_i becomes

$$\tau_i=\alpha_0\tilde{u}_{i-1}^2+\alpha_1\tilde{u}_i^2+\alpha_2\tilde{u}_{i+1}^2+\alpha_3\tilde{u}_{i-1}\tilde{u}_i+\alpha_4\tilde{u}_i\tilde{u}_{i+1}+\alpha_5\tilde{u}_{i+1}\tilde{u}_{i-1}. \tag{11}$$

We would like to point out that the coefficients α_k are sole functions of the stretching factors d_n. In other words, if one can specify the values of d_n in advance, the SGS stress (τ) could be explicitly written in terms of the coarse-grained (resolved) velocity field ($\tilde{u}_i$) weighted according to weights α_k uniquely determined by d_n. In Table I, we have listed the α_k values corresponding to eight stretching factor combinations, $|d_n|=0.887, 0.676$. It is evident that any two combinations (d_1,d_2) and (d_2,d_1) are simply "mirror" images of each other in terms of α_k. Thus, only four distinct multiaffine SGS models (M1, M2, M3, and M4) could be formed from the aforementioned eight $|d_n|$ combinations and in each case the orderings could be chosen at random with equal probabilities. In this table, we have also included the fractal model of [6,7] and the similarity model of [33] in expanded form similar to the multiaffine models (see the Appendix for more information on standard SGS models). The multiaffine models and the fractal model differ slightly in terms of filtering operation. Scotti and Meneveau [6,7] performed filtering at a scale Δ [see Eq. (A4a)], whereas in the case of the similarity model, Liu *et al.* [34] found that it is more appropriate to filter at 2Δ. For the multiaffine models, we also chose to employ the 2Δ filtering scale.

One noticable feature in Table I is that some combinations of d_n result in strongly asymmetric weights α_k. As an example, in the case of M4 with $d_1=+0.676$ and $d_2=+0.887$, $|\alpha_0|\gg|\alpha_2|$ and $|\alpha_3|\gg|\alpha_4|$. This means that the SGS stress at any node x_i would have more weight from the resolved velocity at node x_{i-1} than node x_{i+1}. One would expect that such an asymmetry could have serious implication in terms of SGS model performance.

In the following section, we will attempt to address this issue among others by evaluating several SGS models via the *a priori* analysis approach.

V. EVALUATION OF SGS MODELS: *A PRIORI* ANALYSIS APPROACH

The SGS models and their underlying hypotheses can be evaluated by two approaches: *a priori* testing and *a posteriori* testing (terms coined by [35]). In *a posteriori* testing, LES computations are actually performed with proposed SGS models and validated against reference solutions (in terms of mean velocity, scalar and stress distributions, spectra, etc.). However, owing to the multitude of factors involved in any numerical simulation (e.g., numerical discretizations, time integrations, averaging, and filtering), *a posteriori* tests in general do not provide much insight about the detailed physics of the newly implemented SGS models [26,27]. A complementary and perhaps more fundamental approach [26] would be to use high-resolution model [direct numerical simulation (DNS)], experimental or field observational data to compute the "real" and modeled SGS tensors directly from their definitions and compare them subsequently. This approach, widely known as the *a priori* analysis, does not require any actual LES modeling and is theoretically more tractable. In this work we focused on comparing the performance of SGS models via the *a priori* analysis. We strictly followed the 1D *a priori* analysis approach of [36–38]. To highlight the caveats of the proposed and several existing SGS models, we performed an extensive intermodel comparison study. This exercise also helped to select the "right" combination of stretching factors for the multiaffine SGS models.

TABLE I. The multiaffine, fractal, and similarity SGS models in expanded form and their corresponding coefficients for the computation of SGS stresses according Eq. (11).

Model	(d_1, d_2)	Filter width	α_0	α_1	α_2	α_3	α_4	α_5
Multiaffine (M1)	$(-0.887, +0.676)$	2Δ	0.218	0.204	0.050	−0.372	−0.036	−0.065
	$(+0.676, -0.887)$	2Δ	0.050	0.204	0.218	−0.036	−0.372	−0.065
Multiaffine (M2)	$(+0.887, -0.676)$	2Δ	0.030	0.248	0.261	−0.018	−0.479	−0.043
	$(-0.676, +0.887)$	2Δ	0.261	0.248	0.030	−0.479	−0.018	−0.043
Multiaffine (M3)	$(-0.887, -0.676)$	2Δ	0.144	0.220	0.133	−0.230	−0.209	−0.057
	$(-0.676, -0.887)$	2Δ	0.133	0.220	0.144	−0.209	−0.230	−0.057
Multiaffine (M4)	$(+0.887, +0.676)$	2Δ	0.064	0.319	0.262	−0.121	−0.517	−0.007
	$(+0.676, +0.887)$	2Δ	0.262	0.319	0.064	−0.517	−0.121	−0.007
Fractal	$(-0.794, +0.794)$	Δ	0.127	0.221	0.026	−0.322	−0.120	+0.069
	$(+0.794, -0.794)$	Δ	0.026	0.221	0.127	−0.120	−0.322	+0.069
Similarity	NA	2Δ	0.188	0.250	0.188	−0.250	−0.250	−0.125

In general, the correlation between real (τ^{real}) and modeled (τ^{model}) SGS stresses is considered to be a good indicator of the expected performance of a proposed SGS model. Another crucial indicator is the so-called SGS energy dissipation rate (Π),

$$\Pi = -\tau_{ij}\tilde{S}_{ij} \approx -\frac{15}{2}\tau\frac{\partial \tilde{u}}{\partial x}(\text{1D approximation}). \qquad (12)$$

In the inertial range, the SGS energy dissipation rate is the most influential factor affecting the dynamical evolution of the resolved kinetic energy [26]. On average, Π is positive, representing a net drain of resolved kinetic energy into unresolved motion. Intermittent negative values of Π, known as "backscatter," imply energy transfer from SGS to resolved scales. Unfortunately, a high correlation between real and modeled SGS stress (or SGS energy dissipation rate) is not a sufficient condition for the success of a proposed LES SGS model, although it is a highly desirable feature [27,34,36].

We primarily made use of an extensive atmospheric boundary layer (ABL) turbulence dataset (comprised of fast-response sonic anemometer data) collected by various researchers from the Johns Hopkins University, the University of California–Davis, and the University of Iowa during Davis 1994, 1995, 1996, 1999, and Iowa 1998 field studies. Comprehensive description of these field experiments (e.g., surface cover, fetch, instrumentation, and sampling frequency) can be found in [39]. We further augmented this dataset with nocturnal ABL turbulence data from CASES-99 (Cooperative Atmosphere-Surface Exchange Study 1999), a cooperative field campaign conducted near Leon, Kansas during October 1999 [40]. For our analyses, four levels (1.5, 5, 10, and 20 m) of sonic anemometer data from the 60 m tower and the adjacent minitower collected during two intensive observational periods (on the nights of October 17th and 19th) were considered (the sonic anemometer at 1.5 m was moved to the 0.5 m level on October 19th). Briefly, the collective attributes of the field dataset explored in this study are as follows: (i) surface cover: bare soil, grass and beans; (ii) sampling frequency: 18–60 Hz; (iii) sampling period: 20–30 min; (iv) sensor height (z): 0.5–20 m; and (v) atmospheric stability (z/L, L is the local Obukhov length): 0 (neutral) to 10 (very stable).

ABL field measurements are seldom free from mesoscale disturbances, wave activities, nonstationarities, etc. The situation could be further aggravated by several kinds of sensor errors (e.g., random spikes, amplitude resolution error, drop outs, discontinuities, etc.). Thus, stringent quality control and preprocessing of field data is of the utmost importance for any rigorous statistical analysis. Our quality control and preprocessing strategies are qualitatively similar to the suggestions of [41]. Specifically, we follow these steps.

(i) Visual inspection of individual data series for detection of spikes, amplitude resolution error, drop outs, and discontinuities. Discard suspected data series from further analyses.

(ii) Adjust for changes in wind direction by aligning sonic anemometer data using 60 s local averages of the longitudinal and transverse component of velocity.

(iii) Partitioning of turbulent-mesoscale motion using discrete wavelet transform (Symmlet-8 wavelet) with a gap scale [42] of 100 s.

(iv) Finally, to check for nonstationarities of the partitioned series, we performed the following step: we subdivided each series in six equal intervals and computed the standard deviation of each subseries ($\sigma_i, i=1:6$). If $\max(\sigma_i)/\min(\sigma_i) > 2$, the series was discarded.

After all these quality control and preprocessing steps, we were left with only 358 "reliable" series for *a priori* analyses. These streamwise velocity series were filtered with a top-hat filter (Δ= 1, 2, 4, or 8 m) and downsampled on the scale of the LES grid (Δ) to obtain the resolved velocity field $\tilde{u}_i$ [43]. In a similar way, the streamwise SGS stress, τ^{real}, was computed from its definition [Eq. (9a)]. Filtering operations were always performed in time and interpreted as 1D spatial filtering in the streamwise direction by means of Taylor's frozen flow hypothesis. The spatial derivatives were also computed from the time derivatives by invoking Taylor's hypothesis: $\partial/\partial x = -1/\langle u\rangle(\partial/\partial t)$, where $\langle u\rangle$ is the mean streamwise velocity.

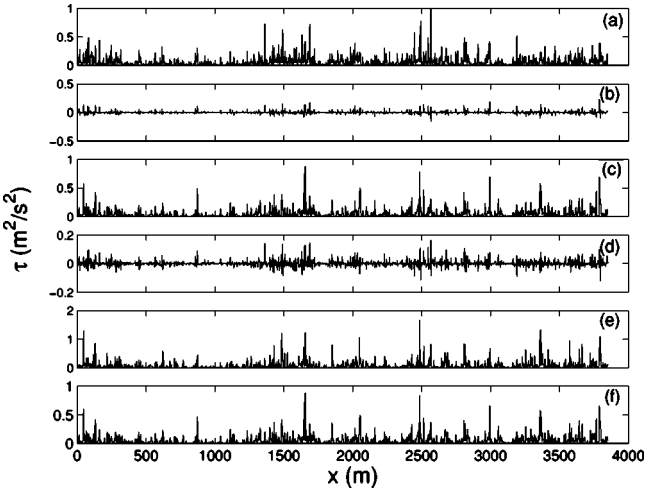

FIG. 4. A comparison of the real and modeled SGS stresses, computed from atmospheric boundary layer measurements, using 1D filtering and Taylor's hypothesis. The filter width Δ is 2 m. (a) Real, (b) Smagorinsky model, (c) similarity model, (d) SGS kinetic-energy-based model, (e) fractal model, and (f) multiaffine model (M3).

In Fig. 4, representative realizations of the real and several modeled SGS stresses are presented. The modeled SGS stresses, τ^{model}, were computed from the definitions given in the Appendix. Along the same lines, the real and modeled SGS energy dissipation rates (Fig. 5) were calculated according to $\Pi^{\text{real}} = -15/2\,\tau^{\text{real}}(\partial\tilde{u}/\partial x)$ and $\Pi^{\text{model}} = -15/2\,\tau^{\text{model}}(\partial\tilde{u}/\partial x)$, respectively. The SGS model constants like C_S of the Smagorinsky model or C_L of the similarity model (see the Appendix) were obtained by matching the mean real and modeled SGS energy dissipation rates [36–38]. For consistency, the same procedure was followed for the SGS-kinetic-energy-based model, fractal model, and

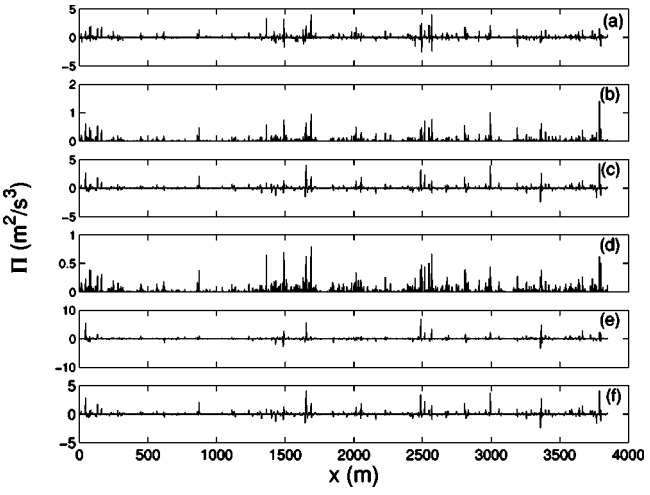

FIG. 5. A comparison of the real and modeled SGS energy dissipation rates, computed from atmospheric boundary layer measurements, using 1D filtering and Taylor's hypothesis. The filter width Δ is 2 m. (a) Real, (b) Smagorinsky model, (c) similarity model, (d) SGS kinetic-energy-based model, (e) fractal model, and (f) multiaffine model (M3).

TABLE II. Average correlation between observed and modeled SGS stresses and energy dissipation rates ($\Delta = 1$ m). The results are based on 358 ABL turbulent velocity series measured during several field campaigns. The quantities in the parentheses represent standard deviation.

	Corr($\tau^{\text{real}}, \tau^{\text{model}}$)	Corr ($\Pi^{\text{real}}, \Pi^{\text{model}}$)
Smagorinsky	0.25(0.09)	0.41(0.17)
Similarity	0.49(0.10)	0.76(0.15)
SGS-KE	0.23(0.08)	0.42(0.17)
Fractal	0.33(0.05)	0.61(0.06)
Multiaffine (M1)	0.44(0.05)	0.71(0.05)
Multiaffine (M2)	0.40(0.05)	0.68(0.06)
Multiaffine (M3)	0.49(0.05)	0.77(0.05)
Multiaffine (M4)	0.42(0.05)	0.70(0.05)

multiaffine models. In other words, we always ensured that $\langle -\frac{15}{2}\tau^{\text{real}}(\partial\tilde{u}/\partial x)\rangle = \langle -\frac{15}{2}\tau^{\text{model}}(\partial\tilde{u}/\partial x)\rangle$. Note that this procedure has no effect on the correlation results presented below. In actual simulations, these model coefficients could be obtained dynamically following the approach of [29,44].

From Fig. 4 and 5 it is visually evident that both similarity and multiaffine models capture the variability of the SGS stress and energy dissipation rates reasonably well. On the other hand, the performances of the Smagorinsky and SGS-kinetic-energy-based models are very poor. Note that the Smagorinsky model assumes that the trace of the SGS tensor is subtracted from the tensor, which is not feasible in 1D *a priori* analysis [36]. Thus, direct magnitude-wise comparison between the real-and the Smagorinsky-model-based SGS stress or dissipation energy is not possible. However, this does not prevent us from quantifying the performance by the correlation coefficient. Moreover, the Smagorinsky model is by construction fully dissipative. Hence, this model is unable to reproduce the backscatter effects [see Fig. 5(b)], which do occur in the real SGS dissipation series [Fig. 5(a)].

In Table II, for $\Delta = 1$ m, we show the correlation between the real and modeled SGS stress and energy dissipation rates. The standard deviations are given in parentheses. The model M3 is significantly better than any other multiaffine model and this could only be attributed to its near-symmetric stencil structure (see Table I). This resolves our previous dilemma regarding the selection of one multiaffine SGS model from a class of four. From here on, we will only report results for M3 and will identify it as the multiaffine model.

Next, in Fig. 6, we plot the mean correlation between real and modeled SGS stress and energy dissipation rates for $\Delta = 1, 2, 4$, and 8 m. As anticipated, for all the models, the correlation decreases with increasing filtering scale. Also, the correlation of real versus model SGS energy dissipation rates is usually higher compared to the SGS stress scenario, as noticed by other researchers.

It is expected that in the ABL the scaling exponent values (ζ_q) would deviate from the values reported in [12] due to the near-wall effect. This means that the stretching factors d_n based on the ζ_q values we used in this work are possibly in error. Nevertheless, the overall performance of the multi-

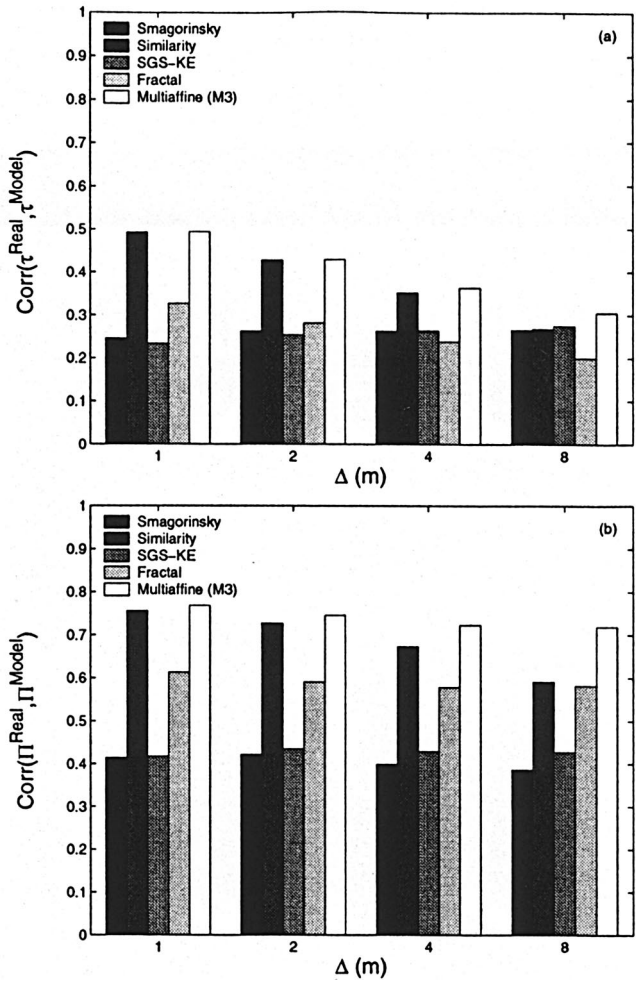

FIG. 6. (a) Correlation between observed and modeled subgrid-scale stresses and (b) correlation between observed and modeled subgrid-scale energy dissipations as a function of filter width Δ. The results are based on 358 ABL turbulent velocity series measured during several field campaigns.

affine model is beyond our expectations. It remains to be seen how the proposed SGS scheme will perform in *a posteriori* analysis, and such work is currently in progress.

VI. PASSIVE SCALAR

Our scheme could be easily extended to synthetic passive-scalar (any diffusive component in a fluid flow that has no dynamical effect on the fluid motion itself, e.g., a pollutant in air, temperature in a weakly heated flow, a dye mixed in a turbulent jet, or moisture mixing in air [45,46]) field generation. The statistical and dynamical characteristics (anisotropy, intermittency, PDFs, etc.) of passive scalars are surprisingly different from the underlying turbulent velocity field [45,46]. For example, it is even possible for the passive-scalar field to exhibit intermittency in a purely Gaussian velocity field [45,46]. Similar to the K41, neglecting intermittency, the Kolmogorov-Obukhov-Corrsin (KOC) hypothesis predicts that at high Reynolds and Peclet numbers, the qth-order passive-scalar structure function will behave as $\langle|\theta(x+r)-\theta(x)|^q\rangle \sim r^{q/3}$ in the inertial range. Experimental observations reveal that analogous to turbulent velocity, passive scalars also exhibit anomalous scaling (departure from the KOC scaling). Observational data also suggest that passive-scalar fields are much more intermittent than velocity fields and result in stronger anomaly [45,46].

To generate synthetic passive-scalar fields, we need to determine the stretching parameters d_1 and d_2 from prescribed scaling exponents, ζ_q. Unlike the velocity scaling exponents, the published values (based on experimental observations) of higher-order passive-scalar scaling exponents display significant scatter. Thus for our purpose, we used the predictions of a newly proposed passive-scalar model [47]: $\zeta_q = 2 + (\frac{8}{9})^2 - 2(\frac{3}{4})^{q/6} - (\frac{8}{9})^2(\frac{7}{16})^{q/2}$. This model based on the hierarchical structure theory of [23] shows reasonable agreement with the observed data. Moreover, unlike other models, this model manages to predict that the scaling exponent ζ_q is a nondecreasing function of q. Theoretically, this is crucial because, otherwise, if $\zeta_q \to -\infty$ as $q \to +\infty$, the passive-scalar field cannot be bounded [12,47].

Employing Eq. (6) and the scaling exponents (up to eighth order) predicted by the above model, we get the following stretching factors: $|d_n| = 0.964, 0.606$. We again repeated the numerical experiment of Sec. III and selected the stretching parameter combination: $d_1 = -0.964$ and $d_2 = 0.606$. Like before, we compared the estimated [using Eq. (4)] scaling exponents from 100 realizations with the theoretical values [from Eq. (6)] and the agreement was found to be highly satisfactory. To check whether a generated passive-scalar field ($d_1 = -0.964$, $d_2 = 0.606$) possesses more non-Gaussian characteristics than its velocity counterpart ($d_1 = -0.887$, $d_2 = 0.676$), we performed a simple numerical experiment. We generated both the velocity and passive-scalar fields from identical anchor points and also computed the corresponding flatness factors, K, as a function of distance r [see Fig. 7(b)]. Comparing Fig. 7(a) with Fig. 3(b) and also from Fig. 7(b), one could conclude that the passive-scalar field exhibits stronger non-Gaussian behavior than the velocity field, in accord with the literature.

VII. CONCLUDING REMARKS

In this paper, we propose a simple yet efficient scheme to generate synthetic turbulent velocity and passive-scalar fields. This method is competitive with most of the other synthetic turbulence emulator schemes (e.g., [1–5]) in terms of capturing small-scale properties of turbulence and scalars (e.g., multiaffinity and non-Gaussian characteristics of the PDF of velocity and scalar increments). Moreover, extensive *a priori* analyses of field measurements unveil the fact that this scheme could be effectively used as a SGS model in LES. Potentially, the proposed multiaffine SGS model can address two of the unresolved issues in LES: it can systematically account for the near-wall and atmospheric stability effects on the SGS dynamics. Of course, this would require some kind of universal dependence of the scaling exponents on both wall-normal distance and stability. The quest for this kind of universality began only recently [48,49].

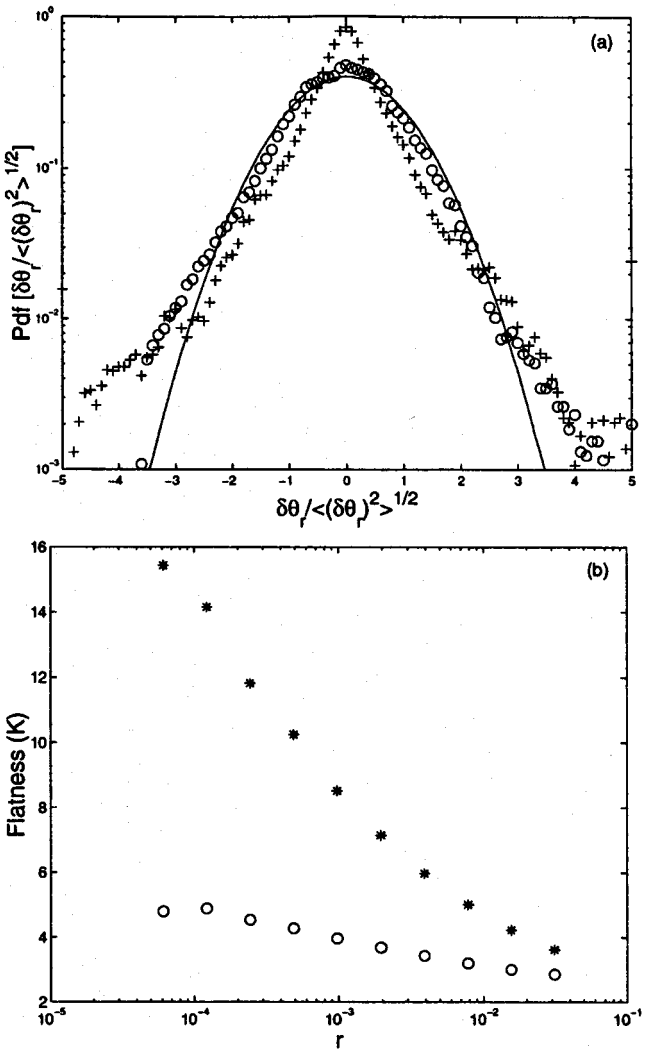

FIG. 7. (a) PDFs of the normalized increments of the passive scalar multiaffine series. The plus signs refer to distance $r=2^{-14}$, while the circles to a distance $r=2^{-6}$. The solid curve designates the Gaussian distribution for reference. (b) The flatness factors of the PDFs of the increments of the velocity (circles) and passive-scalar field (stars) as a function of distance r. Note that both the fields approach the Gaussian value of 3 only at large separation distances. Clearly the passive-scalar field is more non-Gaussian than the velocity field.

ACKNOWLEDGMENTS

We thank Alberto Scotti, Charles Meneveau, Andrea Mazzino, Venugopal Vuruputur, and Boyko Dodov for useful discussions. The first author is indebted to Jacques Lévy-Véhel for his generous help. This work was partially funded by research grants to the principal investigators [NSF (ATM-0130394) and NASA (NAG5-12909, NAG5-13639) to E. F.-G.; NSF (EAR-0094200) and NASA (NAG5-10569, NAG5-11801) to F. P.-A.; and by the STC program of the National Science Foundation under agreement number EAR-0120914 (National Center for Earth-Surface Dynamics). S.B. was partially supported by the University of Minnesota]. All the computational resources were kindly provided by the Minnesota Supercomputing Institute. All this support is greatly appreciated.

APPENDIX

The standard Smagorinsky eddy-viscosity model is of the form

$$\tau_{ij}^{\mathrm{Smag}} = -2(C_S\Delta)^2|\widetilde{S}|\widetilde{S}_{ij}, \tag{A1a}$$

where

$$\widetilde{S}_{ij} = \frac{1}{2}\left(\frac{\partial \widetilde{u}_i}{\partial x_j} + \frac{\partial \widetilde{u}_j}{\partial x_i}\right)$$

is the resolved strain rate tensor and

$$|\widetilde{S}| = (2\widetilde{S}_{ij}\widetilde{S}_{ij})^{1/2}$$

is the magnitude of the resolved strain rate tensor. C_S is the so-called Smagorinsky coefficient.

For 1D surrogate SGS stress,

$$\widetilde{S}_{11} = \frac{\partial \widetilde{u}}{\partial x}.$$

Further, by assuming that the smallest scales of the resolved motion are isotropic, the following equality holds [50]:

$$\langle \widetilde{S}_{ij}\widetilde{S}_{ij}\rangle = \frac{15}{2}\langle \widetilde{S}_{11}^2\rangle.$$

Employing this assumption for the instantaneous fields, we can write

$$|\widetilde{S}| = (2\widetilde{S}_{ij}\widetilde{S}_{ij})^{1/2} \approx \sqrt{15}\left|\frac{\partial \widetilde{u}}{\partial x}\right|.$$

Hence, the Smagorinsky SGS stress equation becomes

$$\tau^{\mathrm{Smag}} = -2(C_S\Delta)^2\sqrt{15}\left|\frac{\partial \widetilde{u}}{\partial x}\right|\left(\frac{\partial \widetilde{u}}{\partial x}\right). \tag{A1b}$$

The second model we considered is the similarity model [33,34],

$$\tau_{ij}^{\mathrm{siml}} = C_L(\overline{\widetilde{u}_i\widetilde{u}_j} - \overline{\widetilde{u}}_i\,\overline{\widetilde{u}}_j). \tag{A2a}$$

The overbar denotes explicit filtering with a filter of width $\gamma\Delta$ (usually $\gamma=2$). C_L is the similarity model coefficient.

The 1D surrogate SGS stress could be simply written as

$$\tau^{\mathrm{siml}} = C_L(\overline{\widetilde{u}\widetilde{u}} - \overline{\widetilde{u}}\,\overline{\widetilde{u}}). \tag{A2b}$$

Now, for 2Δ filtering this equation becomes

$$\tau^{\mathrm{siml}} = C_L\left[\left(\frac{\widetilde{u}_{i-1}^2 + 2\widetilde{u}_i^2 + \widetilde{u}_{i+1}^2}{4}\right) - \left(\frac{\widetilde{u}_{i-1} + 2\widetilde{u}_i + \widetilde{u}_{i+1}}{4}\right)^2\right] \tag{A2c}$$

which on further simplification leads to the expression in Table I,

$$\tau^{\mathrm{siml}} = C_L[0.188\widetilde{u}_{i-1}^2 + 0.25\widetilde{u}_i^2 + 0.188\widetilde{u}_{i+1}^2 - 0.25\widetilde{u}_{i-1}\widetilde{u}_i - 0.25\widetilde{u}_i\widetilde{u}_{i+1} - 0.125\widetilde{u}_{i+1}\widetilde{u}_{i-1}].$$

Next, we consider a SGS model based on the SGS kinetic energy (q^2) [36,51],

$$\tau^{\mathrm{Stke}} = -2C_K^2\Delta\sqrt{|q^2|}\frac{\partial \tilde{u}}{\partial x}, \tag{A3}$$

where

$$q^2 = 3(u-\tilde{u})^2.$$

Here, C_K is the SGS model coefficient.

In the case of the fractal model of [6,7], the unknown subgrid stress (τ) produced by a synthetic fractal field around any grid point x_i can be written as

$$\tau_i^{\mathrm{frac}} = \int_{1/4}^{3/4}[u(x)]^2dx - \left(\int_{1/4}^{3/4}u(x)dx\right)^2 \tag{A4a}$$

$$= \frac{1}{12}(\delta_i\tilde{u})^2 + \frac{d_i(8-3d_i^2)}{48}\delta_i^2\tilde{u}\,\delta_i\tilde{u} + \frac{1+15d_i^2-24d_i^4+12d_i^6}{192(1-d_i^2)}(\delta_i^2\tilde{u})^2, \tag{A4b}$$

where $\delta_i\tilde{u}=(\tilde{u}_{i+1}-\tilde{u}_{i-1})/2$, $\delta_i^2\tilde{u}=\tilde{u}_{i+1}-2\tilde{u}_i+\tilde{u}_{i-1}$, and $d_i = \pm 2^{-1/3}$.

[1] T. Vicsek and A. L. Barabási, J. Phys. A **24**, L845 (1991).
[2] R. Benzi, L. Biferale, A. Crisanti, G. Paladin, M. Vergassola, and A. Vulpiani, Physica D **65**, 352 (1993).
[3] A. Juneja, D. P. Lathrop, K. R. Sreenivasan, and G. Stolovitzky, Phys. Rev. E **49**, 5179 (1994).
[4] L. Biferale, G. Boffetta, A. Celani, A. Crisanti, and A. Vulpiani, Phys. Rev. E **57**, R6261 (1998).
[5] T. Bohr, M. H. Jensen, G. Paladin, and A. Vulpiani, *Dynamical Systems Approach to Turbulence* (Cambridge University Press, Cambridge, UK, 1998).
[6] A. Scotti and C. Meneveau, Phys. Rev. Lett. **78**, 867 (1997).
[7] A. Scotti and C. Meneveau, Physica D **127**, 198 (1999).
[8] M. F. Barnsley, Constructive Approx. **2**, 303 (1986).
[9] M. F. Barnsley, *Fractals Everywhere* (Academic, Boston, MA, 1993).
[10] A. Scotti, C. Meneveau, and S. G. Saddoughi, Phys. Rev. E **51**, 5594 (1995).
[11] K. R. Sreenivasan and R. A. Antonia, Annu. Rev. Fluid Mech. **29**, 435 (1997).
[12] U. Frisch, *Turbulence: The Legacy of A. N. Kolmogorov* (Cambridge University Press, Cambridge, UK, 1995).
[13] F. Anselmet, Y. Gagne, E. J. Hopfinger, and R. A. Antonia, J. Fluid Mech. **140**, 63 (1984).
[14] G. Parisi and U. Frisch, in *Proceedings of the International School on Turbulence and Predictability in Geophysical Fluid Dynamics and Climate Dynamics*, edited by M. Ghil, R. Benzi, and G. Parisi (North-Holland, Amsterdam, 1985).
[15] G. G. Katul, J. D. Albertson, C. R. Chu, and M. B. Parlange, in *Wavelets in Geophysics*, edited by E. Foufoula-Georgiou and P. Kumar (Academic, San Diego, 1994).
[16] J. Lévy-Véhel, K. Daoudi, and E. Lutton, Fractals **2**, 1 (1994).
[17] J. F. Muzy, E. Bacry, and A. Arneodo, Phys. Rev. E **47**, 875 (1993).
[18] S. Jaffard, SIAM J. Math. Anal. **28**, 944 (1997).
[19] E. Bacry, A. Arneodo, U. Frisch, Y. Gagne, and E. Hopfinger, in *Turbulence and Coherent Structures*, edited by O. Métais and M. Lesieur (Kluwer, Dordrecht, 1990).
[20] M. Vergassola, R. Benzi, L. Biferale, and D. Pisarenko, J. Phys. A **26**, 6093 (1993).
[21] B. Mandelbrot, *Fractals: Form, Chance, and Dimension* (Freeman, New York, 1977).
[22] A. Davis, A. Marshak, W. Wiscombe, and R. Cahalan, J. Geophys. Res. **99**, 8055 (1994).
[23] Z. S. She and E. L. Lévêque, Phys. Rev. Lett. **72**, 336 (1994).
[24] In most of today's LES computations, the filtering operation is basically implicit. This means that the process of numerical discretization (of grid size Δ) in itself creates the filtering effect. Although explicit filtering of the grid-resolved velocity field is desirable from a theoretical point of view, limited computational resources make it impractical [25] . However, in *a priori* studies of DNS, experimental, or field observations, where fine resolution velocity fields are readily available, the explicit filtering (typically with a top hat, Gaussian or cutoff filter) followed by downsampling is usually performed to compute the resolved (and filtered) velocity $\tilde{u}_i$. This issue of filtering of velocity fields should not be confused with the explicit filterings done in the cases of similarity, dynamic, fractal, or multiaffine models to compute the SGS stresses or other necessary SGS tensors.
[25] G. L. Eyink, e-print chao-dyn/9602019.
[26] C. Meneveau and J. Katz, Annu. Rev. Fluid Mech. **32**, 1 (2000).
[27] P. Sagaut, *Large Eddy Simulation for Incompressible Flows* (Springer-Verlag, Berlin, 2001).
[28] J. Smagorinsky, Mon. Weather Rev. **91**, 99 (1963).
[29] M. Germano, U. Piomelli, P. Moin, and W. Cabot, Phys. Fluids A **3**, 1760 (1991).
[30] F. Porté-Agel, C. Meneveau, and M. B. Parlange, J. Fluid Mech. **415**, 216 (2000).
[31] M. Antonelli, A. Mazzino, and U. Rizza, J. Atmos. Sci. **60**, 215 (2003).
[32] J. A. Domaradzki and N. A. Adams, J. Turbul. **3**, 1 (2002).
[33] J. Bardina, J. H. Ferziger, and W. C. Reynolds, AIAA J. **80**, 1357 (1980).
[34] S. Liu, C. Meneveau, and J. Katz, J. Fluid Mech. **275**, 83 (1994).
[35] U. Piomelli, P. Moin, and J. H. Ferziger, Phys. Fluids **31**, 1884 (1988).
[36] C. Meneveau, Phys. Fluids **6**, 815 (1994).
[37] J. O'Neil and C. Meneveau, J. Fluid Mech. **349**, 253 (1997).
[38] F. Porté-Agel, C. Meneveau, and M. B. Parlange, Boundary-Layer Meteorol. **88**, 425 (1998).
[39] M. Pahlow, M. B. Parlange, and F. Porté-Agel, Boundary-Layer Meteorol. **99**, 225 (2001).
[40] G. S. Poulos and Coauthors, Bull. Am. Meteorol. Soc. **83**, 555 (2002).

[41] D. Vickers and L. Mahrt, J. Atmos. Ocean. Technol. **14**, 512 (1997).
[42] D. Vickers and L. Mahrt, J. Atmos. Ocean. Technol. **20**, 660 (2003).
[43] Following [34], this filtering followed by downsampling methodology is known in the literature as "consistent" *a priori* analysis.
[44] D. K. Lilly, Phys. Fluids A **4**, 633 (1992).
[45] Z. Warhaft, Annu. Rev. Fluid Mech. **32**, 203 (2000).
[46] B. I. Shraiman and E. D. Siggia, Nature (London) **405**, 639 (2000).
[47] Q. Z. Feng, Phys. Fluids **14**, 2019 (2002).
[48] G. Ruiz-Chavarria, S. Ciliberto, C. Baudet, and E. Lévêque, Physica D **141**, 183 (2000).
[49] K. G. Aivalis, K. R. Sreenivasan, Y. Tsuji, J. C. Klewicki, and C. A. Biltoft, Phys. Fluids **14**, 2439 (2002).
[50] A. Monin and A. Yaglom, *Statistical Fluid Mechanics* (MIT Press, Cambridge, MA, 1971).
[51] V. C. Wong, Phys. Fluids A **4**, 1081 (1992).